



Quantum metrology via chaos in a driven Bose-Josephson system

Wenjie Liu ^{1,2}, Min Zhuang,^{1,2} Bo Zhu,¹ Jiahao Huang,^{1,*} and Chaohong Lee ^{1,2,3,†}

¹Guangdong Provincial Key Laboratory of Quantum Metrology and Sensing & School of Physics and Astronomy, Sun Yat-Sen University (Zhuhai Campus), Zhuhai 519082, China

²State Key Laboratory of Optoelectronic Materials and Technologies,

Sun Yat-Sen University (Guangzhou Campus), Guangzhou 510275, China

³Synergetic Innovation Center for Quantum Effects and Applications, Hunan Normal University, Changsha 410081, China



(Received 14 July 2020; revised 29 November 2020; accepted 27 January 2021; published 8 February 2021)

Entanglement preparation and signal accumulation are essential for quantum parameter estimations, which pose significant challenges to both theories and experiments. Here, we propose how to utilize chaotic dynamics in a periodically driven Bose-Josephson system for achieving high-precision measurements beyond the standard quantum limit (SQL). Starting from an initial nonentangled state, the chaotic dynamics generates many-body quantum entanglement and simultaneously encodes the parameter to be estimated. By using suitable chaotic dynamics, the ultimate measurement precision of the estimated parameter can beat the SQL. The sub-SQL measurement precision scaling can also be reached via specific observables, such as collective spin measurement, which can be realized with state-of-art techniques. Our study not only provides insights for understanding quantum chaos and quantum-classical correspondence, but also of promising applications in entanglement-enhanced quantum metrology.

DOI: [10.1103/PhysRevA.103.023309](https://doi.org/10.1103/PhysRevA.103.023309)

I. INTRODUCTION

Quantum metrology promises high-precision measurements for various parameters with far-reaching implications for science and technology [1–3]. In general, the standard procedure of parameter estimation consists of three stages: Initialization, parameter-dependent time evolution, and measurement [4]. In traditional protocols, for separable initial states [5,6], i.e., nonentangled states, the related measurement precision scales as the standard quantum limit (SQL), which is inversely proportional to the square root of particle number \sqrt{N} , while for entangled initial states, e.g., the Greenberger-Horne-Zeilinger (GHZ) state [7–9] or NOON state [10–12], the measurement precision can be improved to the well-known Heisenberg limit (HL), which is inversely proportional to N .

Thus, in the long-standing quest for achieving high-precision measurements, a key goal as well as a main challenge is to prepare the entangled states and make use of the entanglement to improve measurement precision. On one hand, entangled states often require a lot of time to generate, which makes it hard to prepare [13–17]. On the other hand, the entangled states are extremely fragile under the environmental noises, which inevitably decreases the measurement precision [18–20].

Recently, to fully utilize the temporal resources, schemes on concurrent entanglement generation and interrogation are proposed [21,22]. Different from the traditional protocols where interrogation takes place after state preparation,

the concurrent state preparation and interrogation devote all the time for parameter encoding, which yields a better measurement precision under the same temporal resource [21]. In particular, by combining the conventional one-axis twisting (OAT) dynamics with a machined-designed sequence of rotations, a higher sensitivity of the estimated parameter can be achieved compared with traditional schemes [22].

Classical chaos, a well-defined property in nonlinear dynamical systems, is generally characterized by exponential instability due to sensitivity to the initial conditions [23–26]. On the other hand, entanglement is a unique property of quantum systems [27]. Up to now, numerous works aim to find out the connections between chaos and entanglement [28–31]. It has been explored mostly in the semiclassical regime through studies of various models such as the quantum kicked top [32–34], Bose-Josephson junction [35,36], Dicke model [37–39], Bose-Hubbard model [40–42], and so on. These studies are beneficial not only for the fundamental understanding of quantum-classical correspondence, but also for implications in quantum metrology where entanglement is used as an important resource [43].

Chaotic behaviors, as an entanglement-generating dynamics, have the potential to enhance the measurement precision. In a kicked top with a Dirac-delta driving, one finds chaotic behaviors can be employed to realize a high-precision parameter estimation according to the analysis of the quantum Fisher information (QFI) and Fisher information (FI) [44]. Ultimate measurement precision can be substantially enhanced by nonlinearly kicking the spin during the parameter-encoding precession and driving it into a chaotic regime. However, despite its simplicity, such a discontinuous driving is not easy to realize [45].

*hjiahao@mail2.sysu.edu.cn

†lichao2@mail.sysu.edu.cn

Periodically continuous time-dependent modulation allows one to manipulate a quantum system in a controlled way, which is more feasible in experiments. For example, a harmonically driven Bose-Josephson system is also a suitable platform for studying quantum chaotic dynamics. This is what motivates us to propose a chaotic quantum metrology scheme based on the harmonic driving in a Bose-Josephson system. Naturally, based on a driven Bose-Josephson system, the following questions are worth considering: (i) Is it possible to utilize a more experimentally feasible continuous driving for chaotic generation and use it for entanglement-enhanced quantum metrology? (ii) Can the ultimate measurement precision scaling reach beyond the SQL? (iii) Can we find a suitable realistic observable measurement for measurement precision scaling to demonstrate our scheme?

In this paper, we study the chaotic dynamics in a harmonically driven Bose-Josephson system, and demonstrate how to make use of the chaotic behaviors to achieve a measurement precision beyond the SQL. Unlike the conventional parameter estimation schemes, we initialize the system into a spin coherent state (SCS) and let it undergo a chaotic dynamics governed by a parameter-dependent Hamiltonian. During the time evolution, not only is an entangled final state generated via chaotic dynamics, but also the estimated parameter is encoded into the final state, which can effectively improve the measurement precision. We employ a mean-field approximation to arrive at classical Poincaré sections and then identify the parameter regime at which chaotic seas appear. Classical chaos facilitates our search for its quantum counterparts, such as linear entropy, fidelity, and QFI. By appropriately choosing the initial states, the scaling analysis of QFI reveals that chaos contributes to measurement precision enhancement. More specifically, a sub-SQL N scaling can be extracted from FI as well as a collective spin measurement.

This paper is organized as follows. In Sec. II, we briefly describe the harmonically driven Bose-Josephson system. In Sec. III, we show how to perform quantum parameter estimation in the considered system. In Sec. IV, we derive the approximate mean-field Hamiltonian in the classical limit, and calculate the corresponding Poincaré sections to identify the locations of the chaotic seas with several different system parameters. In Sec. V, under the guidance of quantum counterparts, we verify that QFI, FI, and collective spin measurement all exhibit an excellent N scaling. In Sec. VI, we give a brief summary and discussion.

II. A HARMONICALLY DRIVEN BOSE-JOSEPHSON SYSTEM

We are interested in a driven Bose-Josephson system whose time-dependent Hamiltonian reads

$$\hat{H}(t)/\hbar = \hat{H}_1 + \hat{H}_2(t), \quad (1)$$

with the linear term

$$\hat{H}_1 = B_z \hat{S}_z, \quad (2)$$

and the nonlinear driven term

$$\hat{H}_2(t) = \frac{\chi}{N} \hat{S}_z^2 + B_x \cos \omega t \hat{S}_x. \quad (3)$$

Here, B_z is the strength of the static longitudinal magnetic field, χ denotes the nonlinear interaction coupling strength, and $B_x \cos \omega t$ represents a harmonically driven transverse magnetic field with the modulation amplitude B_x and the modulation frequency ω . N is the total particle number of the system. Throughout the paper, for convenience, we set $\omega = 2\pi$ and $\hbar = 1$.

The Bose-Josephson system can be regarded as a spin- J system comprising N spin-1/2 particles with a pseudospin length $J = N/2$. The corresponding collective spin operators are defined as $\hat{S}_x = (\hat{b}_2^\dagger \hat{b}_1 + \hat{b}_1^\dagger \hat{b}_2)/2$, $\hat{S}_y = (\hat{b}_2^\dagger \hat{b}_1 - \hat{b}_1^\dagger \hat{b}_2)/2i$, and $\hat{S}_z = (\hat{b}_2^\dagger \hat{b}_2 - \hat{b}_1^\dagger \hat{b}_1)/2$, where \hat{b}_μ (\hat{b}_μ^\dagger) is the atom annihilation (creation) operator and $\hat{n}_\mu = \hat{b}_\mu^\dagger \hat{b}_\mu$ is the occupation operator in mode μ . Therefore, the Hamiltonian (1) is equivalent to the Hamiltonian of a two-mode Bose-Hubbard model

$$\begin{aligned} \hat{H}_{\text{BH}} = & \frac{\chi}{4N} (\hat{n}_2 - \hat{n}_1)^2 + \frac{B_z}{2} (\hat{n}_2 - \hat{n}_1) \\ & + \frac{B_x \cos \omega t}{2} (\hat{b}_2^\dagger \hat{b}_1 + \hat{b}_1^\dagger \hat{b}_2), \end{aligned} \quad (4)$$

with $N = \langle \hat{N} \rangle = \langle \hat{n}_1 + \hat{n}_2 \rangle$ representing the atom number N . Since $[\hat{N}, \hat{H}_{\text{BH}}] = 0$, the total number of atoms N is conserved. $\{|J, m_z\rangle\}$, called the Dicke basis, are common eigenstates of \hat{S}^2 and \hat{S}_z with eigenvalues $J(J+1)$ and m_z . In the Dicke basis $\{|J, m_z\rangle\}$ with $m_z = -J, -J+1, \dots, J$, arbitrary quantum states of the Hamiltonian (1) can be written as $|\Psi\rangle = \sum_{m_z} C_{m_z} |J, m_z\rangle$, where C_{m_z} denotes the probability amplitude projecting onto the basis $|J, m_z\rangle$. Under the condition $\omega = 0$, if the system is dominated by the transverse magnetic field B_x , the ground state is the SU(2) SCS. For a positive nonlinearity strength which is large enough, the ground state turns to $|J, 0\rangle$ for even N or $(|J, 1/2\rangle + |J, -1/2\rangle)/\sqrt{2}$ for odd N , while if negative nonlinearity strength dominates, two degenerate ground states $|J, J\rangle$ and $|J, -J\rangle$ appear and any superposition of these two states is a ground state, including the GHZ state $(|J, J\rangle + |J, -J\rangle)/\sqrt{2}$.

III. QUANTUM PARAMETER ESTIMATION

A longitudinal magnetic field causes a precession about the z axis. The strength of the longitudinal magnetic field B_z is the parameter we want to estimate. Assuming other parameters are known, we are interested in the measurement precision of B_z . Generally, quantum parameter estimation can be described by a positive-operator valued measure (POVM) comprising a set of positive Hermitian operators \hat{E}_n , which satisfy $\hat{E}_n \geq 0$ and $\sum_n \hat{E}_n = \mathbf{1}$, and n denotes the outcome of the measurement. Starting from an initial nonentangled state $|\psi_0\rangle$, the system can be driven to undergo chaotic dynamics while the estimated parameter B_z is encoded into the evolved state. The entangled output state satisfies $|\psi_f(B_z)\rangle = \hat{U} |\psi_0\rangle$ with the time-evolution operator

$$\hat{U} = \hat{T} \exp \left[-i \int_{t_0}^t \hat{H}(t') dt' \right] \quad (5)$$

governed by the whole system (1). Here, \hat{H}_1 encodes the estimated parameter B_z . At the same time, \hat{H}_2 acts as an OAT Hamiltonian which can be exploited to prepare the squeezed states as well as rotate the system around the x axis with

a continuous driving. Both terms in the stroboscopic time evolution conspire to provide a high-precision measurement from an initial nonentangled state.

By reading out the final state, the conditional probability of the measurement result given by the estimated parameter B_z yields

$$P_n = \langle \psi_f | \hat{E}_n | \psi_f \rangle. \quad (6)$$

The FI related to the conditional probability reads as

$$F_I(B_z) = \sum_n P_n \left(\frac{\partial \ln P_n}{\partial B_z} \right)^2. \quad (7)$$

For a given POVM, the Cramér-Rao bound is expressed as

$$\Delta B_z \geq 1/\sqrt{\mathcal{N}F_I}, \quad (8)$$

which gives the minimal achievable uncertainty of the estimated parameter with \mathcal{N} times trials. FI represents an ability to measure the parameter and instructs one to enhance the measurement precision by maximizing it. Maximizing the FI by trying all possible POVM, it is known that the ultimate measurement precision is limited by the quantum Cramér-Rao bound

$$\Delta B_z \geq 1/\sqrt{\mathcal{N}F_Q}. \quad (9)$$

The corresponding FI with the optimal POVM measurement is called a QFI. The QFI can be calculated as

$$F_Q(B_z) = 4[\langle \psi'_f | \psi'_f \rangle - |\langle \psi'_f | \psi_f \rangle|^2], \quad (10)$$

where $|\psi'_f\rangle = \partial|\psi_f\rangle/\partial B_z$ denotes the derivative of the final state with respect to the estimated parameter B_z . Obviously, the QFI is only depends on the final state as well as its derivative.

We consider two typical states as initial states, the SCS and GHZ states. The initial SCS reads in the Dicke basis as

$$|J, \theta, \phi\rangle = \sum_{m_z=-J}^J \sqrt{\binom{2J}{J+m_z}} \sin(\theta/2)^{J+m_z} \times \cos(\theta/2)^{J-m_z} e^{i(J+m_z)\phi} |J, m_z\rangle, \quad (11)$$

with θ and ϕ as the polar and azimuthal angles, respectively. Correspondingly, the GHZ state is expressed as $(|J, J\rangle + |J, -J\rangle)/\sqrt{2}$. For conventional parameter estimation schemes, the linear term \hat{H}_1 serves as the parameter-dependent time evolution and one can use the entangled input state to enhance the measurement precision. In the absence of $\hat{H}_2(t)$, the system dynamics is dominated by \hat{H}_1 . After substituting the initial states and the evolved Hamiltonian \hat{H}_1 into Eq. (10), the QFIs can be calculated. Mathematically, for an initial SCS $|N/2, \theta, \phi\rangle$, $F_Q = Nt^2 \sin^2 \theta$. When $\theta = \pi/2$, corresponding to all individual spins in equal superposition among the two levels, the QFI is the optimal, i.e., $F_Q = Nt^2 \equiv F_{\text{SQL}}$, while for an initial GHZ state, the corresponding QFI becomes $F_Q = N^2 t^2 \equiv F_{\text{HL}}$. As for the references, $\Delta B_z \geq 1/\sqrt{F_{\text{SQL}}} = 1/(\sqrt{N}t)$ is the SQL, while $\Delta B_z \geq 1/\sqrt{F_{\text{HL}}} = 1/(Nt)$ is the HL.

IV. MEAN-FIELD APPROXIMATION

First, we should know the conditions for generating chaos and then try to perform the measurement by using the chaotic behaviors. To study the properties of chaos, we employ the mean-field theory to obtain a classical Hamiltonian equation. We then examine its Poincaré sections, especially for identifying the parameter regime at which chaotic behaviors appear. For Hamiltonian (4), in the semiclassical limit $N \rightarrow \infty$, the whole system is dominated by the condensed atoms and can be approached via the mean-field approximation, i.e., $\hat{b}_\mu \approx \psi_\mu$, $\hat{b}_\mu^\dagger \approx \psi_\mu^*$, with $\psi_\mu = \langle \hat{b}_\mu \rangle$, $\psi_\mu^* = \langle \hat{b}_\mu^\dagger \rangle$. The total particle number $|\psi_1|^2 + |\psi_2|^2 = N$ is conserved. Applying the mean-field approximation, the classical Hamiltonian equation is written as

$$H_{\text{MF}} = \frac{\chi}{4N} (n_2 - n_1)^2 + \frac{B_z}{2} (n_2 - n_1) + \frac{B_x \cos \omega t}{2} (\psi_1^* \psi_2 + \psi_2^* \psi_1). \quad (12)$$

Substituting the mean-field Hamiltonian (12) into the equation

$$i\hbar \frac{d\psi_\mu(t)}{dt} = \frac{\partial H_{\text{MF}}}{\partial \psi_\mu^*(t)}, \quad (13)$$

the two coupled differential equations yield

$$i \frac{d\psi_1}{dt} = -\frac{B_z}{2} \psi_1 + \frac{\chi}{2N} (|\psi_1|^2 - |\psi_2|^2) \psi_1 + \frac{B_x \cos \omega t}{2} \psi_2, \\ i \frac{d\psi_2}{dt} = +\frac{B_z}{2} \psi_2 + \frac{\chi}{2N} (|\psi_2|^2 - |\psi_1|^2) \psi_2 + \frac{B_x \cos \omega t}{2} \psi_1. \quad (14)$$

The complex amplitudes can be expressed as $\psi_\mu = \sqrt{n_\mu} \exp(i\phi_\mu)$ in terms of the particle number $n_\mu = \psi_\mu^* \psi_\mu$ and the phase ϕ_μ . Due to two degrees of freedom lying in the system, one can further set up two canonical variables, the fractional population imbalance $z = \frac{n_1 - n_2}{N} = \cos \theta$ and the relative phase $\phi = \phi_1 - \phi_2$. The equations of motion in parameter space (ϕ, z) are given by

$$\frac{d\phi}{dt} = z\chi - \frac{zB_x \cos \omega t}{\sqrt{1-z^2}} \cos \phi - B_z, \\ \frac{dz}{dt} = B_x \cos \omega t \sqrt{1-z^2} \sin \phi. \quad (15)$$

We numerically obtain the Poincaré sections by recording the phase space locations at each integer multiple of period T .

The mean-field approach enables us to locate parameter regimes at which chaotic and regular regions coexist or chaotic behaviors dominate. Once such parameter regime is identified, and we then explore the difference between initial states locating in different regions. Through plotting the Poincaré sections, we get the trajectory of the system up to 500 periods for different transverse magnetic field strengths B_x : 0, 1.5, 3, and 5.5, as depicted in Fig. 1. Here, the particle number is $N = 1000$, the longitudinal magnetic field strength is $B_z = \pi/2$, and the nonlinearity strength is $\chi = 10$.

In the absence of a transverse magnetic field, the regular behaviors perfectly emerge in the whole phase space [see Fig. 1(a)]. Once the transverse magnetic field is added, in addition to the regular behaviors, the chaotic behaviors

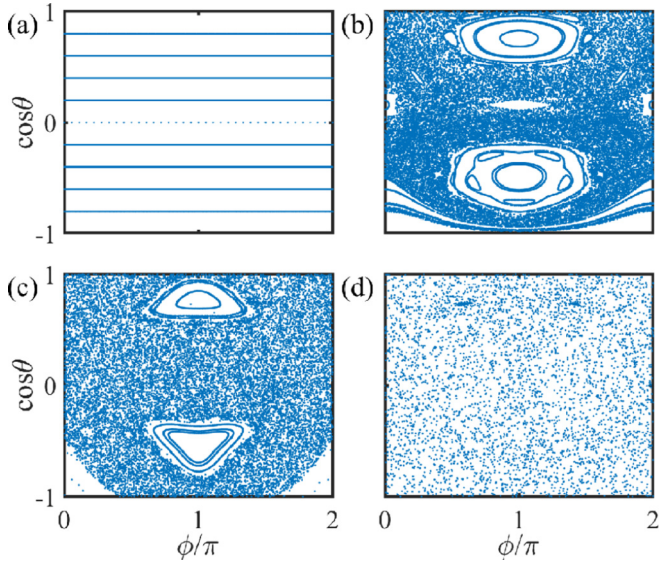


FIG. 1. Poincaré sections governed by Eq. (15) at different strengths of the transverse magnetic field: (a) $B_x = 0$, (b) $B_x = 1.5$, (c) $B_x = 3$, and (d) $B_x = 5.5$. The other parameters are chosen as $N = 1000$, $\chi = 10$, and $B_z = \pi/2$.

also appear [see Fig. 1(b)]. When B_x increases further, the chaotic regions enlarge while the regular regions shrink [see Fig. 1(c)]. Up to a sufficiently large $B_x = 5.5$, the chaotic regions nearly dominate [see Fig. 1(d)]. In addition, we note that these Poincaré sections are almost symmetric about the line $\phi = \pi$, and it allows us to just concentrate on its left part.

V. FULL QUANTUM APPROACH

The periodically driven system (1) respects a discrete translation symmetry in the time domain, $\hat{H}(t + T) = \hat{H}(t)$ with a Floquet period $T = 2\pi/\omega$. \hat{T} is the time-ordering operator, and the time-evolution operator in a single period can be calculated as

$$\hat{U}(T; 0) = \hat{T} \exp\left(-i \int_0^T \hat{H}(t) dt\right) \equiv \exp(-i\hat{H}_F T). \quad (16)$$

The system stroboscopic dynamics at moments nT ($n = 1, 2, \dots$) is governed by the time-averaged Hamiltonian

$$\hat{H}_F = \frac{i}{T} \ln \hat{U}(T; 0). \quad (17)$$

So far, we map the time-dependent system (1) to a time-independent one (17), and one can obtain the stroboscopic time evolution from the static Hamiltonian \hat{H}_F . The periodically modulated transverse magnetic field flexibly controls the system behaviors. The interplay between the nonlinearity strength and modulation amplitude may generate the chaotic behaviors for a fixed modulation frequency, which will be discussed later.

The chaotic behaviors are closely related to entanglement generation. We devote ourselves to searching for suitable quantum counterparts to find the connections to the corresponding chaos. Then, we also calculate the corresponding QFI, which can be used as a measure for the precision bounds of the estimated parameter. We find that, after a long-time

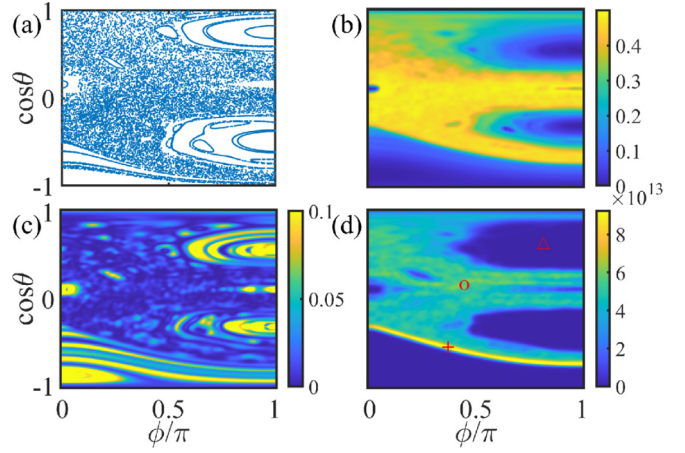


FIG. 2. (a) Poincaré section as a function of θ, ϕ corresponding to Fig. 1(b). (b)–(d) Its corresponding phase space distributions of linear entropy, fidelity, and QFI in the quantum setting exemplarily for a system with a large particle number ($N = 1000$) up to $t = 2^{15}T$. The other parameters are chosen as $\chi = 10$, $B_x = 1.5$, and $B_z = \pi/2$. Marks labeled in (d) are chosen as initial parameters in Fig. 3.

evolution, the QFI for the chaotic region will be much larger than the one for the regular region. Furthermore, by choosing initial coherent states in different regions, we evaluate the scalings of QFI versus evolution time t and total particle number N . The N scaling of QFI with chaotic dynamics can exceed the SQL. To demonstrate our scheme from the perspective of experimental realization, for the case of mostly chaotic phase space, we also analyze the scalings of practical observables, such as FI and collective spin measurement.

A. In mixed phase space

First, we study the quantum counterparts of classical phase space in which chaotic regions coexist with regular regions and analyze the scalings of QFI. Due to the symmetry of the Poincaré section about the line $\phi = \pi$, it is reasonable to just take into account the case for ϕ ranging from 0 to π , as shown in Fig. 2(a). In order to explore the whole evolution of the quantum counterparts, all points in the Poincaré section are taken as initial states to evolve. Numerically, we deal with the time-evolution operator $\hat{U}(T; 0)$ by a series of discrete time steps $\delta t = T/1000$, and then let the system evolve in a time domain with the static Hamiltonian \hat{H}_F .

Entropy, as a pure quantum resource, is a powerful bridge between the classical and quantum worlds. The linear entropy characterizes the entanglement between a single particle and the rest of the system defined as

$$S(nT) = \frac{1}{2} \left(1 - \frac{\langle \hat{S}_x \rangle^2 + \langle \hat{S}_y \rangle^2 + \langle \hat{S}_z \rangle^2}{J^2} \right) \quad (18)$$

at the stroboscopic time nT ($n = 1, 2, \dots, N$). The linear entropy nicely reproduces a similar structure to the Poincaré section [see Fig. 2(b)]. The regions of classical phase space where the dynamics is chaotic correspond to high entropy in the quantum system. Regions that are classically regular correspond to low entropy. Related works [46–48] have found the striking resemblance between the entanglement in the

quantum system and chaos in the classical limit. From the analysis of the linear entropy, we know the entanglement can be dynamically generated by the chaotic dynamics scheme.

The fidelity is written as

$$F(nT) = |\langle \psi(0) | \psi(nT) \rangle|^2, \quad (19)$$

which is used to quantify how much information could remain in the time-evolved state $|\psi(nT)\rangle$ comparing to the initial state $|\psi(0)\rangle$. References [49,50] have proposed the dynamical properties can serve as the signatures of chaotic behavior such as coherence dynamics and temporal fluctuations. Similarly, the fidelity serves as a dynamically sensitive probe for distinguishing the chaotic sea and regular island from the perspective of the difference between the initial and final states. The initial SCS distributes in the Bloch sphere with a localized form. In the regular region, one would get a perfect localization nature and the state would remain trapped in the regular island for all times, whereas the initial SCS centered in the chaotic region tends to undergo an ergodic dynamics, thus losing a lot of local information in a final state with low fidelity. A good quantum-classical correspondence is exhibited via fidelity [see Fig. 2(c)]. The linear entropy and fidelity not only both establish a good correspondence between the quantum dynamics and classical phase space, but they also present a complementary relationship, that is, the chaotic regions are indicated by the small value of fidelity and high entropy, while a large value of fidelity and low entropy implies regular regions.

The generated entanglement can be exploited for metrology, which explains how chaos contributes to the enhancement of measurement precision. More directly, we calculate the corresponding QFI, which is closely related to quantum parameter estimation according to Eq. (9). A similar structure reflects that the classical dynamics of the system has an excellent correspondence with the quantum dynamics of QFI, in Fig. 2(d). After a long-time evolution, the final QFIs arising from the initial states in chaotic or regular regions are obviously different. A chaotic sea takes on a large QFI while a regular island possesses a relatively small QFI. Remarkably, the border between the chaotic sea and regular island, called an edge state, has a larger QFI. We refer to these three typical regions as a chaotic sea (circle), edge state (cross), and regular island (triangle), which are marked in Fig. 2(d).

The distributions of final states in the Bloch sphere reveal an ergodic dynamics for a chaotic sea or edge state and a localized dynamics for a regular island (see Appendix A for more details). It is shown that a linear entropy, fidelity, and QFI can all be used as sensitive probes for the quantum-classical correspondence of chaos. In comparison with the classical Poincaré section, these quantum counterparts may not only distinguish regular and chaotic regions, but also present much richer results by quantifying the chaos from different perspectives.

In order to investigate the role of chaos in parameter estimation, still within the mixed phase space, we adopt the initial parameters in different regions in Fig. 2(d) to explore their differences, from the perspective of QFI. In Fig. 3, different marks correspond to the different states initially prepared in the locations shown in Fig. 2(d). Figure 3(a) shows, beginning from a moderate evolved time, that QFI still increases with

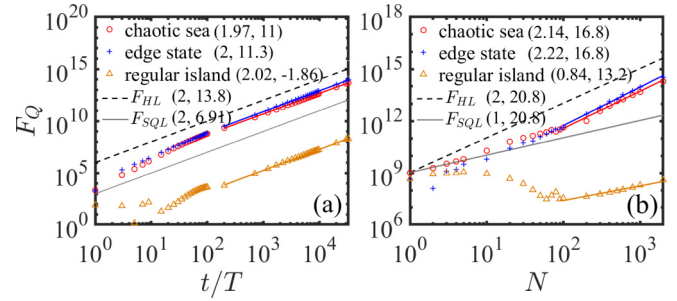


FIG. 3. QFI with respect to t and N for different initial parameters. (a) The stroboscopic evolution of QFI up to 2^{15} periods with a system size $N = 1000$. The fitted results (S, C) satisfy $\ln(F_Q) = S \ln(t/T) + C$ with a slope S and a constant C . Fits exhibit a chaotic sea (1.97, 11), edge state (2, 11.3), and regular island (2.02, -1.86) for t scaling. (b) QFI for different N with a fixed evolution time $t = 2^{15}T$. The fitted results (S, C) satisfy $\ln(F_Q) = S \ln(N) + C$ with a slope S and a constant C . Fits exhibit a chaotic sea (2.14, 16.8), edge state (2.22, 16.8), and regular island (0.84, 13.2) for N scaling. The other parameters are chosen as $\chi = 10$, $B_x = 1.5$, and $B_z = \pi/2$. The gray solid line and black dashed line represent the SQL and HL, respectively.

t and shows a nearly quadratic t scaling for chaotic, edge, and regular initial situations. When an initial state locates on a chaotic sea (circle) or edge state (cross), QFI evolves with time between the SQL and HL, while for an initial state locating within a regular island (triangle), QFI evolves below the SQL. In addition, we note that the edge state is superior to a chaotic sea all the time. The evolved time as a resource is able to improve its value of QFI.

For a fixed evolution time $t = 2^{15}T$, Fig. 3(b) reflects that the N scaling of QFI is sensitive to the locations of the initial states. Besides the early decay in a regular region, QFIs increase with the particle number N for chaotic, edge, and regular situations. The numerical results reveal that an initial state in a chaotic sea performs best for small N , while for a larger system size ($N > 100$) the edge state performs best. Fits for three different initial states take on a slope of 2.14 (chaotic sea), 2.22 (edge state), and 0.84 (regular island) for the N scaling. Both N scalings for an edge state and chaotic sea can approach even better than HL while an initial state in a regular island fails to beat the SQL. It is indicated that chaos as a kind of resource allows one to attain a high-precision measurement beyond the SQL.

It has been already known that quantum metrology aims to utilize quantum effects to enhance the parameter measurement precision such as entanglement [1–3]. The comparison of QFI with linear entropy in Figs. 2(b) and 2(d) shows that QFI rapidly grows accompanied by the generation of linear entropy. Starting from the initial SCS without entanglement, the state gradually evolves into an entangled under the ergodic dynamics in a chaos sea and edge regime which has the potential to improve the estimation precision. However, for an initial state in regular islands, the system undergoes periodic dynamics with a relatively high fidelity with its initial SCS yielding a SQL [see Fig. 2(c)] and the corresponding linear entropy and QFI behave similarly with the SCS [see Figs. 2(b) and 2(d)].

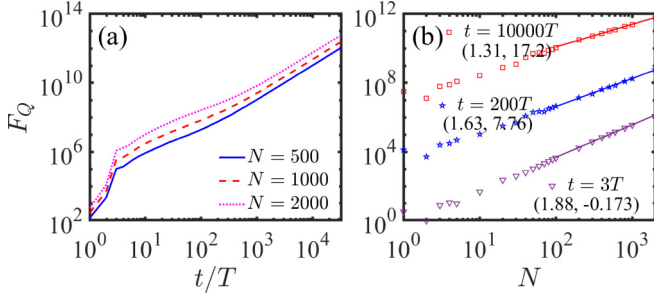


FIG. 4. (a) QFI as a function of stroboscopic evolution time with different system sizes $N = 500$ (solid line), 1000 (dashed line), and 2000 (dotted line) in a fully chaotic regime. (b) QFI as a function of system sizes for different evolution times. The fitted results (S, C) satisfy $\ln(F_Q) = S \ln(N) + C$ with a slope S and a constant C . Fits exhibit $t = 3T$ (1.88, -0.173), $t = 200T$ (1.63, 7.76), and $t = 10000T$ (1.31, 17.2) for N scaling. The initial state locates on $\theta = 2.423$, $\phi = 1.126$. The other parameters are chosen as $\chi = 10$, $B_x = 5.5$, and $B_z = \pi/2$.

B. In a fully chaotic regime

According to the scaling analysis in the mixed phase space, we have known that chaotic behaviors can play an important role for quantum parameter estimation. Next, we naturally turn to the fully chaotic regime, and evaluate the scalings for QFI with respect to t and N . In particular, as the system enters full chaos, the information about the initial SCS is rapidly lost. Therefore the initial SCS can be chosen anywhere without much changing the QFI, and the situation is markedly different from the case of a mixed phase space.

Below we focus on the phase space of QFI whose classical counterpart displays fully chaotic behaviors corresponding to Fig. 1(d). Independent of the details of the initial state, we randomly choose the initial parameters as $\theta = 2.423$, $\phi = 1.126$. In the fully chaotic case ($\chi = 10$, $B_x = 5.5$, and $B_z = \pi/2$), the numerical results in Fig. 4(a) depict a time evolution of QFI for different system sizes, which manifests as QFI drastically increases during a short evolution time ($t \simeq 3T$) and behaves similarly at three different system sizes: $N = 500$, 1000, and 2000. For a large N , QFI is more sensitive to the early time. Since we take a SCS as the initial state, the value of QFI is small at the initial time. As the evolution time increases, the evolved state rapidly spreads out on the phase space because of the ergodic dynamics in a chaotic sea which results in a high-level entanglement. Compared with traditional OAT dynamics, our chaotic dynamics can speed up the entanglement generation (see Appendix B for more details). After the initial rapid growth, QFI grows slowly for a long time.

In order to further explore the influence of the evolution time, we calculate the N scalings of QFI in Fig. 4(b) for different evolution times: $t = 3T$, $200T$, and $10000T$. Other parameters agree with the Poincaré section shown in Fig. 1(d). Figure 4(b) displays the N scaling of QFI nearly achieves HL for a short evolution time ($t \simeq 3T$), then gradually decays to SQL with increasing evolution time.

In principle, QFI corresponds to the optimal POVM measurement and just mathematically sets the ultimate bound of the measurement precision, but it may not always be

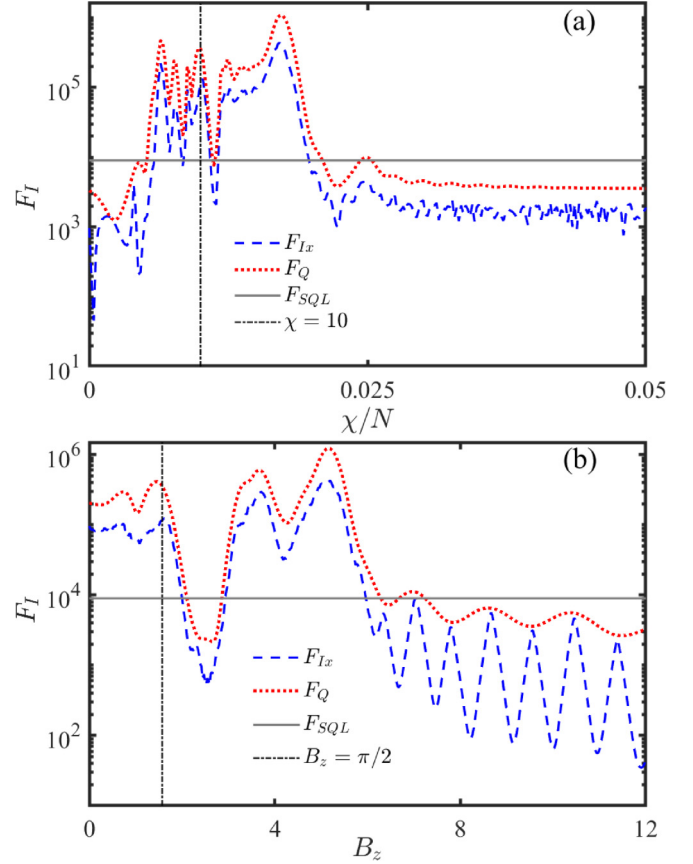


FIG. 5. QFI and FI of the collective spin operator \hat{S}_x (a) as a function of χ for $B_z = \pi/2$ and (b) as a function of B_z for $\chi = 10$. The initial state locates on $\theta = 2.423$, $\phi = 1.126$, and $B_x = 5.5$. The evolution time is $t = 3T$ and the system size is chosen as $N = 1000$. The gray solid line represents the SQL.

realistic. To approach the precision bounds set by QFI, we specify a feasible measurement, i.e., FI (7). Starting from a given initial state $|J, \theta, \phi\rangle$, where θ and ϕ signify the position of the SCS, the estimated parameter B_z is encoded into the evolved state during a stroboscopic evolution. The Dicke basis $\{|J, m_\alpha\rangle\}$ comprises the common eigenstates of \hat{S}^2 and \hat{S}_α for $m_\alpha = -J, -J + 1, \dots, J$ with $\alpha = x, y, z$. The obtained final state can be written in the Dicke basis as $|\psi_f\rangle = \sum_{m_\alpha=-J}^J C_{m_\alpha}(B_z) |J, m_\alpha\rangle$. The conditional probabilities related to the collective spin operator \hat{S}_α can be calculated as $P(m_\alpha|B_z) = |C_{m_\alpha}(B_z)|^2$, and its FI is defined as

$$F_{I\alpha}(B_z) = \sum_{m_\alpha} \frac{1}{|C_{m_\alpha}(B_z)|^2} \left(\frac{\partial |C_{m_\alpha}(B_z)|^2}{\partial B_z} \right)^2. \quad (20)$$

Considering the parameter dependence of QFI and FI, we are devoted to analyzing the QFI and FI versus χ in Fig. 5(a) and QFI and FI vs B_z in Fig. 5(b). Based on the aforementioned experience in Fig. 4, we consider the system size $N = 1000$ and perform a time evolution up to $t = 3T$. By calculating the FI related to collective spin operator \hat{S}_x , one finds FI outperforms the SQL in a certain region of nonlinearity strength χ in Fig. 5(a) as well as in a broad range of B_z in Fig. 5(b) but always below its QFI, which includes our

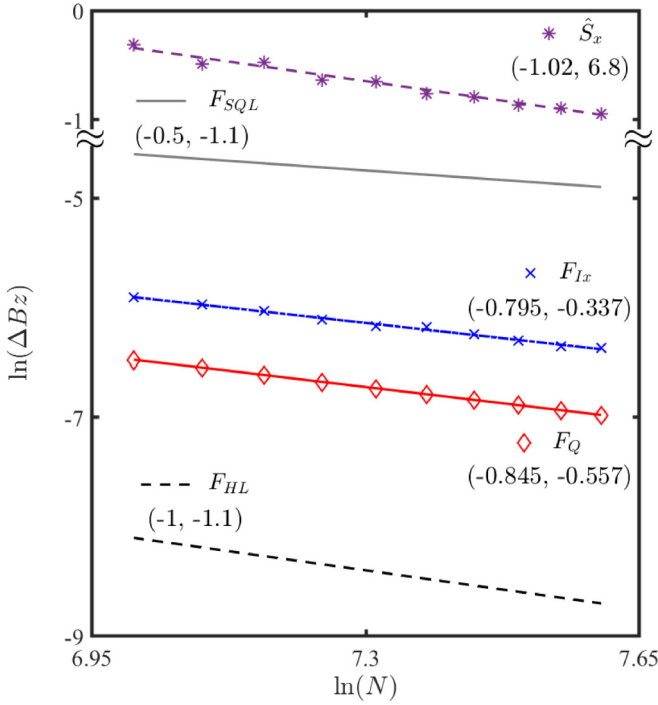


FIG. 6. The log-log plot of the measurement-precision scaling obtained from \hat{S}_x , F_{Ix} , F_Q , F_{SQL} , and F_{HL} . The fitted results (S, C) satisfy $\ln(\Delta B_z) = S \ln(N) + C$ with a slope S and a constant C . The system size takes a value from $N = 1000$ to 2000 . The other parameters are chosen as $\chi = 10$, $B_z = \pi/2$, and $B_x = 5.5$. The initial state locates on $\theta = 2.423$, $\phi = 1.126$, and the evolution time is $t = 3T$.

discussed case $\chi = 10$ and $B_z = \pi/2$ marked with the black dashed-dotted lines in Figs. 5(a) and 5(b).

Based on the known results in Fig. 4 and Fig. 5, we proceed to carry out a comparison of N scaling. The measurement precision of FI and QFI is obtained via Eqs. (8) and (9). Besides, we can perform an observable (collective spin) measurement to estimate the final measurement precision. According to the error propagation formula, its measurement precision is given by

$$\Delta B_z = \frac{(\Delta \hat{S}_\alpha)_F}{|\partial \langle \hat{S}_\alpha \rangle_F / \partial B_z|}, \quad (21)$$

where $\langle \hat{S}_\alpha \rangle_F = \langle \Psi_F | \hat{S}_\alpha | \Psi_F \rangle$ denotes the expectation value and $(\Delta \hat{S}_\alpha)_F = \sqrt{\langle \Psi_F | \hat{S}_\alpha^2 | \Psi_F \rangle - \langle \Psi_F | \hat{S}_\alpha | \Psi_F \rangle^2}$ is the corresponding standard deviation for $\alpha = x, y, z$. The state before the measurement can be written as $|\Psi_F\rangle = e^{-i\frac{\pi}{2}\hat{S}_x}|\psi_f\rangle$. This $\pi/2$ pulse is applied to the evolved final state for recombination.

Here, we select the collective spin measurement \hat{S}_x as the observable for evaluation. Choosing the particle number from $N = 1000$ to 2000 , a $\ln(\Delta B_z)$ - $\ln(N)$ scaling is shown in Fig. 6. These fits yield slopes of -1.02 (\hat{S}_x), -0.795 (F_{Ix}), -0.845 (F_Q), -0.5 (F_{SQL}), and -1 (F_{HL}) for N scaling. From the N scalings of F_{Ix} and F_Q , it is obvious that the chaotic dynamics exhibits the ability to beat the SQL, and the ultimate precision bound can be approached by detecting the FI. By contrast, the measurement precision obtained by the practical collective spin measurement deviates from the ultimate bound. However, its precision scaling is approximately proportional to N^{-1} ,

which attains the HL except for a large constant. Overall, we provide numerical evidence that the ultimate achievable precision obtained by QFI strictly outperforms the SQL. In addition, not only can a high-precision parameter estimation be realized via the FI, but also a Heisenberg-limited log-log scaling can be obtained via the collective spin measurement, which may be verified in experiments.

VI. SUMMARY AND DISCUSSION

Based on a harmonically driven Bose-Josephson system, we propose a dynamic high-precision measurement scheme, which generates quantum entanglement via chaos and simultaneously encodes the parameter to be estimated. Our scheme not only overcomes the challenges of entangled state preparation, but also utilizes the most of the temporal resources. To better understand the connection between chaotic behaviors and metrology, we make a qualitative comparison between the classical Poincaré section and full quantum approach of the linear entropy, fidelity, and QFI. These three quantum counterparts well reflect the coexistence of chaotic and regular regions from different perspectives. More specifically, we respectively choose three different initial states in the mixed phase space and compare their ultimate precision scalings. The analysis of ultimate precision scalings in mixed phase space indicates that chaos can be used to enhance the measurement precision. Then, we turn to investigate the fully chaotic case. The corresponding QFI and FI both exhibit measurement precision scaling beating the SQL. Finally, we choose the practical collective spin measurement for parameter estimation. Despite the absolute measurement precisions being worse than the precision bounds set by QFI and FI, the precision scalings can still beat the SQL.

Besides, we briefly discuss the experimental feasibility. The Bose-Josephson system (1) can be experimentally realized via a two-mode Bose-Hubbard system consisting of trapping bosons in two hyperfine levels [51–54]. χ as the atom-atom interaction can be tuned via the Feshbach resonance [55–57]. By applying a time-modulated magnetic field, one may obtain the driven term of $\hat{H}_2(t)$. We start with a SCS $|J, \theta, \phi\rangle$, which is easy to prepare by employing a unitary transformation at the specific angle (θ, ϕ) to the state in which all particles are spin down $|\downarrow\rangle$. In addition, the FI may be experimentally obtained according to the method demonstrated in Ref. [57]. The implemented $\pi/2$ pulse before the

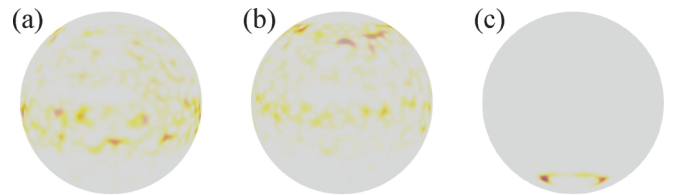


FIG. 7. A distribution comparison of different final states, occurring for different initial states labeled in Fig. 2(d). Different from the wide spreading in a generalized Bloch sphere for a chaotic sea in (a) and edge state in (b), the regular dynamics is restricted in a localized region for regular island in (c).

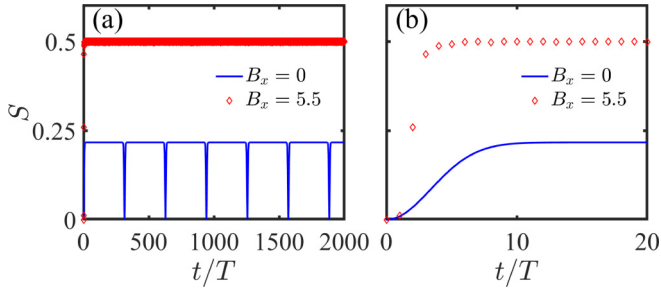


FIG. 8. (a) The linear entropy as a function of evolution time with $B_x = 0$ and $B_x = 5.5$. (b) The enlarged comparison in the early time of (a). The initial state locates on $\theta = 2.423$, $\phi = 1.126$. The other parameters are chosen as $N = 1000$, $\chi = 10$, and $B_z = \pi/2$.

collective spin measurement has also been well developed in synthetic quantum systems [58–60].

It is shown that the chaotic dynamics can contribute to the enhancement of measurement precision. However, decoherence, such as dephasing and dissipation, will be an important ingredient in realistic systems. In practice, it is also worth exploring the influence of chaos dynamics in open quantum systems.

ACKNOWLEDGMENTS

This work is supported by the Key-Area Research and Development Program of GuangDong Province under Grant No. 2019B030330001, the NSFC (Grants No. 12025509, No. 11874434, and No. 11704420), and the Science and Technology Program of Guangzhou (China) under Grant No. 201904020024. J.H. is partially supported by the Guangzhou Science and Technology Projects (202002030459). M.Z. is partially supported by the NSFC (Grant No. 12047563).

APPENDIX A: STATE DISTRIBUTION IN BLOCH SPHERE

The distribution in the Bloch sphere provides a natural way to display the state difference. Based on three different initial parameters labeled in Fig. 2(d), after a long-time evolution up to $t = 2^{15}T$, the obtained final state as well as its density matrix are described by $|\psi_f\rangle$ and $\rho = |\psi_f\rangle\langle\psi_f|$, respectively. One can project the final state $|\psi_f\rangle$ into the Q representation,

$$Q(\theta, \phi) = \frac{2J+1}{4\pi} \langle\theta, \phi|\rho|\theta, \phi\rangle, \quad (\text{A1})$$

then vividly take on the generalized Bloch sphere (see Fig. 7). The initial states in a chaotic region and edge region are scrambled into the entire system and lost their local information during the process of quantum chaos, as shown

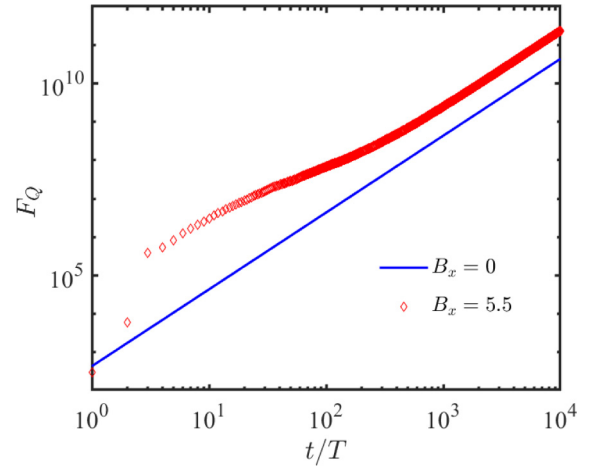


FIG. 9. QFI as a function of evolution time with $B_x = 0$ and $B_x = 5.5$. The initial state locates on $\theta = 2.423$, $\phi = 1.126$. The other parameters are chosen as $N = 1000$, $\chi = 10$, and $B_z = \pi/2$.

in Figs. 7(a) and 7(b), respectively. Compared to a chaotic regime, the distribution of a final state launched from a regular island is restricted within this stability island [see Fig. 7(c)]. A discrepancy is evident for both the regular and chaotic initial SCS.

APPENDIX B: COMPARISON BETWEEN CHAOTIC DYNAMICS AND ONE-AXIS TWISTING DYNAMICS

Here, we compare the entanglement generation between our chaotic dynamics scheme and the traditional one-axis twisting (OAT) scheme, by calculating the linear entropy S (see Fig. 8) and QFI F_Q (see Fig. 9) versus evolution time. For $B_x = 0$ without modulation, it undergoes a traditional OAT dynamics, and the corresponding linear entropy behaves periodically with evolution time [see Fig. 8(a)], while for our chaotic dynamics scheme (the case with modulation strength $B_x = 5.5$), the linear entropy sharply increases to a large value and then nearly remains constant [see Fig. 8(a)]. The maximum linear entropy of chaotic dynamics is much larger than the one in the OAT dynamics. We enlarge the region at a very early time [see Fig. 8(b)]. It is clearly shown that the linear entropy for our chaotic dynamics blows up dramatically in a very short time, while the linear entropy for OAT dynamics grows slowly.

Similarly, the corresponding QFI of chaotic dynamics also shows a rapid increase at a short time and always outperforms the one of OAT dynamics (see Fig. 9). It is evident that, by comparing the linear entropy as well as the QFI versus evolution time for both schemes, our chaotic dynamics can speed up the entanglement generation and further enhance the measurement precision. This advantage can be practical and beneficial for quantum metrology.

- [1] V. Giovannetti, S. Lloyd, and L. Maccone, Quantum-enhanced measurements: Beating the standard quantum limit, *Science* **306**, 1330 (2004).
 [2] V. Giovannetti, S. Lloyd, and L. Maccone, Quantum Metrology, *Phys. Rev. Lett.* **96**, 010401 (2006).

- [3] V. Giovannetti, S. Lloyd, and L. Maccone, Advances in quantum metrology, *Nat. Photonics* **5**, 222 (2011).
 [4] B. M. Escher, R. L. de Matos Filho, and L. Davidovich, General framework for estimating the ultimate precision limit in noisy quantum-enhanced metrology, *Nat. Phys.* **7**, 406 (2011).

- [5] J. M. Radcliffe, Some properties of coherent spin states, *J. Phys. A* **4**, 313 (1971).
- [6] W.-M. Zhang, D. H. Feng, and R. Gilmore, Coherent states: Theory and some applications, *Rev. Mod. Phys.* **62**, 867 (1990).
- [7] D. Bouwmeester, J.-W. Pan, M. Daniell, H. Weinfurter, and A. Zeilinger, Observation of Three-Photon Greenberger-Horne-Zeilinger Entanglement, *Phys. Rev. Lett.* **82**, 1345 (1999).
- [8] W. Dür, G. Vidal, and J. I. Cirac, Three qubits can be entangled in two inequivalent ways, *Phys. Rev. A* **62**, 062314 (2000).
- [9] C. Lee, Adiabatic Mach-Zehnder Interferometry on a Quantized Bose-Josephson Junction, *Phys. Rev. Lett.* **97**, 150402 (2006).
- [10] A. N. Boto, P. Kok, D. S. Abrams, S. L. Braunstein, C. P. Williams, and J. P. Dowling, Quantum Interferometric Optical Lithography: Exploiting Entanglement to Beat the Diffraction Limit, *Phys. Rev. Lett.* **85**, 2733 (2000).
- [11] H. Lee, P. Kok, and J. P. Dowling, A quantum Rosetta stone for interferometry, *J. Mod. Opt.* **49**, 2325 (2002).
- [12] M. Zwiernik, C. A. Pérez-Delgado, and P. Kok, General Optimality of the Heisenberg Limit for Quantum Metrology, *Phys. Rev. Lett.* **105**, 180402 (2010).
- [13] J. Ma, X. G. Wang, C. P. Sun, and F. Nori, Quantum spin squeezing, *Phys. Rep.* **509**, 89 (2011).
- [14] A. D. Ludlow, M. M. Boyd, J. Ye, E. Peik, and P. O. Schmidt, Optical atomic clocks, *Rev. Mod. Phys.* **87**, 637 (2015).
- [15] L. Pezzè, A. Smerzi, M. K. Oberthaler, R. Schmied, and P. Treutlein, Quantum metrology with nonclassical states of atomic ensembles, *Rev. Mod. Phys.* **90**, 035005 (2018).
- [16] J. Huang, M. Zhuang, and C. Lee, Non-Gaussian precision metrology via driving through quantum phase transitions, *Phys. Rev. A* **97**, 032116 (2018).
- [17] J. Huang, M. Zhuang, B. Lu, Y. Ke, and C. Lee, Achieving Heisenberg-limited metrology with spin cat states via interaction-based readout, *Phys. Rev. A* **98**, 012129 (2018).
- [18] R. Demkowicz-Dobrzański, J. Kołodyński, and M. Guţă, The elusive Heisenberg limit in quantum-enhanced metrology, *Nat. Commun.* **3**, 1063 (2012).
- [19] R. Chaves, J. B. Brask, M. Markiewicz, J. Kołodyński, and A. Aïcn, Noisy Metrology beyond the Standard Quantum Limit, *Phys. Rev. Lett.* **111**, 120401 (2013).
- [20] J. Huang, X. Qin, H. Zhong, Y. Ke, and C. Lee, Quantum metrology with spin cat states under dissipation, *Sci. Rep.* **5**, 17894 (2015).
- [21] A. J. Hayes, S. Dooley, W. J. Munro, K. Nemoto, and J. Dunningham, Making the most of time in quantum metrology: Concurrent state preparation and sensing, *Quantum Sci. Technol.* **3**, 035007 (2018).
- [22] S. A. Haine and J. J. Hope, Machine-Designed Sensor to Make Optimal Use of Entanglement-Generating Dynamics for Quantum Sensing, *Phys. Rev. Lett.* **124**, 060402 (2020).
- [23] M. Tabor, *Chaos and Integrability in Nonlinear Dynamics: An Introduction* (Wiley, New York, 1989).
- [24] M. C. Gutzwiller, *Chaos in Classical and Quantum Mechanics*, (Springer, Berlin, 1990).
- [25] R. C. Hilborn, *Chaos and Nonlinear Dynamics*, (Oxford University Press, Oxford, U.K., 2000).
- [26] F. Haake, *Quantum Signatures of Chaos*, 3rd ed. (Springer, Berlin, 2010).
- [27] R. Horodecki, P. Horodecki, M. Horodecki, and K. Horodecki, Quantum entanglement, *Rev. Mod. Phys.* **81**, 865 (2009).
- [28] W. H. Zurek and J. P. Paz, Decoherence, Chaos, and the Second Law, *Phys. Rev. Lett.* **72**, 2508 (1994).
- [29] C. Neill, P. Roushan, M. Fang, Y. Chen, M. Kolodrubetz, Z. Chen, A. Megrant, R. Barends, B. Campbell, B. Chiaro *et al.*, Ergodic dynamics and thermalization in an isolated quantum system, *Nat. Phys.* **12**, 1037 (2016).
- [30] A. Piga, M. Lewenstein, and J. Q. Quach, Quantum chaos and entanglement in ergodic and nonergodic systems, *Phys. Rev. E* **99**, 032213 (2019).
- [31] D. Rosa, D. Rossini, G. Andolina, M. Polini, and M. Carrega, Ultra-stable charging of fast-scrambling SYK quantum batteries, *J. High Energy Phys.* **11** (2020) 067.
- [32] F. Haake, M. Kus, and R. Scharf, Classical and quantum chaos for a kicked top, *Z. Phys. B* **65**, 381 (1987).
- [33] R. Schack, G. M. D'Ariano, and C. M. Caves, Hypersensitivity to perturbation in the quantum kicked top, *Phys. Rev. E* **50**, 972 (1994).
- [34] S. Ghose, R. Stock, P. Jessen, R. Lal, and A. Silberfarb, Chaos, entanglement, and decoherence in the quantum kicked top, *Phys. Rev. A* **78**, 042318 (2008).
- [35] R. Utermann, T. Dittrich, and P. Hänggi, Tunneling and the onset of chaos in a driven bistable system, *Phys. Rev. E* **49**, 273 (1994).
- [36] C. Lee, W. Hai, L. Shi, X. Zhu, and K. Gao, Chaotic and frequency-locked atomic population oscillations between two coupled Bose-Einstein condensates, *Phys. Rev. A* **64**, 053604 (2001).
- [37] P. W. Milonni, J. R. Ackerhalt, and H. W. Galbraith, Chaos in the Semiclassical N -Atom Jaynes-Cummings Model: Failure of the Rotating-Wave Approximation, *Phys. Rev. Lett.* **50**, 966 (1983).
- [38] K. Furuya, M. C. Nemes, and G. Q. Pellegrino, Quantum Dynamical Manifestation of Chaotic Behavior in the Process of Entanglement, *Phys. Rev. Lett.* **80**, 5524 (1998).
- [39] C. Emary and T. Brandes, Chaos and the quantum phase transition in the Dicke model, *Phys. Rev. E* **67**, 066203 (2003).
- [40] A. R. Kolovsky and A. Buchleitner, Quantum chaos in the Bose-Hubbard model, *Europhys. Lett.* **68**, 632 (2004).
- [41] A. R. Kolovsky, Bose-Hubbard Hamiltonian: Quantum chaos approach, *Int. J. Mod. Phys. B* **30**, 1630009 (2016).
- [42] A. Giraldo, B. Krauskopf, N. G. R. Broderick, J. A. Levenson, and A. M. Yacomotti, The driven-dissipative Bose-Hubbard dimer: Phase diagram and chaos, *New J. Phys.* **22**, 043009 (2020).
- [43] J. Huang, S. Wu, H. Zhong, and C. Lee, Quantum metrology with cold atoms, *Annu. Rev. Cold At. Mol.* **2**, 365 (2014).
- [44] L. J. Fiderer and D. Braun, Quantum metrology with quantum-chaotic sensors, *Nat. Commun.* **9**, 1351 (2018).
- [45] P. Nurwantoro, R. W. Bomantara, and J. B. Gong, Discrete time crystals in many-body quantum chaos, *Phys. Rev. B* **100**, 214311 (2019).
- [46] P. A. Miller and S. Sarkar, Signatures of chaos in the entanglement of two coupled quantum kicked tops, *Phys. Rev. E* **60**, 1542 (1999).
- [47] E. Boukobza, M. Chuchem, D. Cohen, and A. Vardi, Phase-Diffusion Dynamics in Weakly Coupled Bose-Einstein Condensates, *Phys. Rev. Lett.* **102**, 180403 (2009).
- [48] E. Boukobza, M. G. Moore, D. Cohen, and A. Vardi, Nonlinear Phase Dynamics in a Driven Bosonic Josephson Junction, *Phys. Rev. Lett.* **104**, 240402 (2010).

- [49] C. Khripkov, D. Cohen, and A. Vardi, Coherence dynamics of kicked Bose-Hubbard dimers: Interferometric signatures of chaos, *Phys. Rev. E* **87**, 012910 (2013).
- [50] C. Khripkov, D. Cohen, and A. Vardi, Temporal fluctuations in the bosonic Josephson junction as a probe for phase space tomography, *J. Phys. A: Math Theor.* **46**, 165304 (2013).
- [51] D. S. Hall, M. R. Matthews, J. R. Ensher, C. E. Wieman, and E. A. Cornell, Dynamics of Component Separation in a Binary Mixture of Bose-Einstein Condensates, *Phys. Rev. Lett.* **81**, 1539 (1998).
- [52] A. Smerzi, A. Trombettoni, T. Lopez-Arias, C. Fort, P. Maddaloni, F. Minardi, and M. Inguscio, Macroscopic oscillations between two weakly coupled Bose-Einstein condensates, *Eur. Phys. J. B* **31**, 457 (2003).
- [53] M. Egorov, R. P. Anderson, V. Ivannikov, B. Opanchuk, P. Drummond, B. V. Hall, and A. I. Sidorov, Long-lived periodic revivals of coherence in an interacting Bose-Einstein condensate, *Phys. Rev. A* **84**, 021605(R) (2011).
- [54] C. Lee, J. Huang, H. Deng, H. Dai, and J. Xu, Nonlinear quantum interferometry with Bose condensed atoms, *Front. Phys.* **7**, 109 (2012).
- [55] C. Gross, T. Zibold, E. Nicklas, J. Estève, and M. K. Oberthaler, Nonlinear atom interferometer surpasses classical precision limit, *Nature (London)* **464**, 1165 (2010).
- [56] W. Muessel, H. Strobel, D. Linnemann, D. B. Hume, and M. K. Oberthaler, Scalable Spin Squeezing for Quantum-Enhanced Magnetometry with Bose-Einstein Condensates, *Phys. Rev. Lett.* **113**, 103004 (2014).
- [57] H. Strobel, W. Muessel, D. Linnemann, T. Zibold, D. B. Hume, L. Pezzè, A. Smerzi, and M. K. Oberthaler, Fisher information and entanglement of non-Gaussian spin states, *Science* **345**, 424 (2014).
- [58] G. de Lange, Z. H. Wang, D. Ristè, V. V. Dobrovitski, and R. Hanson, Universal dynamical decoupling of a single solid-state spin from a spin bath, *Science* **330**, 60 (2010).
- [59] G. de Lange, D. Ristè, V. V. Dobrovitski, and R. Hanson, Single-Spin Magnetometry with Multipulse Sensing Sequences, *Phys. Rev. Lett.* **106**, 080802 (2011).
- [60] P. C. Maurer, G. Kucsko, C. Latta, L. Jiang, N. Y. Yao, S. D. Bennett, F. Pastawski, D. Hunger, N. Chisholm, M. Markham, D. J. Twitchen, J. I. Cirac, and M. D. Lukin, Room-temperature quantum bit memory exceeding one second, *Science* **336**, 1283 (2012).